scientific reports

Check for updates

OPEN

Zero-Power consumption based evaporative cooling for rated current conduction in SiC mosfets

Kuo-Bin Hong[1], Shivendra Kumar Singh[2,5], Chen Sung[3], Yu-Sheng Hsiao[3], Yi-Kai Hsiao[1], Yogesh Singh Chauhan[5], Hao-Chung Kuo[1,6]✉, Tian-Li Wu[2,4,7]✉ & Chang-Ching Tu[1,8]✉

This work demonstrates a highly efficient, zero-power-consumption evaporative cooling system for managing heat generated by SiC MOSFETs operating near their current capacity. The system employs capillary-driven water transport through cotton ropes to an aluminum heatsink, where cellulose paper spreads the water for even evaporation. The process effectively lowers the junction temperature (T_j) of the MOSFETs, monitored in real-time using the correlation between its on-resistance (R_{ON}) and T_j. Evaporative cooling dissipates 42% of total heat without a fan and 89% with a fan. COMSOL simulations are performed and can closely match experimental data, highlighting that optimizing heat transfer between the lead frame and heatsink and increasing the cooling fin height are the keys to further improve the evaporative cooling efficiency. This study offers a sustainable and efficient cooling solution for high-power SiC MOSFETs, reducing reliance on energy-intensive cooling systems and demonstrating potential scalability for industrial applications.

Keywords Evaporative cooling, SiC mosfets, Thermal management, Zero-Power consumption, COMSOL

Owing to the high breakdown electric field and high thermal conductivity of SiC, metal-oxide-semiconductor field-effect transistors based on SiC (SiC MOSFETs) have recently found widespread applications in the 800-V powertrain traction inverters of electric vehicles, for which high power, high efficiency and high-power density are necessary[1–3]. Compared to conventional insulated gate bipolar transistors based on Si (Si IGBTs), the SiC MOSFETs have about 10 times thinner epitaxial layers and much lower turn-off switching loss because of unipolar conduction. As a result, the SiC MOSFETs can offer higher efficiency and higher power density compared to Si IGBTs, achieving peak efficiency up to 99% and power density more than 40 kW/L for electric vehicle traction inverters[4,5]. On the other hand, compared to lateral GaN high electron mobility transistors (GaN HEMTs), the SiC MOSFETs are vertical and based on homoepitaxial layers, thus exhibiting much better voltage-blocking capability and hard switching reliability[6,7].

Inadequate cooling can lead to serious thermal reliability issues. In general, SiC MOSFET-based inverter modules of electric vehicles use liquid-cooling systems, in which water flows through a heatsink to dissipate heat, enabling cooling in high power density[8]. However, this setup requires additional components like pumps, tubing and coolant, further increasing weight, complexity and cost. Furthermore, the pump's power consumption reduces overall efficiency, and inadequate water flow rates may lead to hotspots, especially under high loads. Recently, double-sided cooling, which dissipates heat from both sides of the module, has shown the potential to achieve more uniform temperature distribution and lower thermal resistance. When paired with advanced packaging technologies, such as silver sintering, this approach can further improve cooling efficiency and enable thinner and lower-inductance designs[9,10]. However, double-sided cooling requires intricate thermal management on both sides[11,12], often involving specialized bonding materials that add potential reliability challenges due to unmatched thermal expansion and stress at interconnects[13,14].

[1]Semiconductor Research Center, Hon Hai Research Institute, Taipei, Taiwan. [2]International College of Semiconductor Technology, National Yang Ming Chiao Tung University, Hsinchu, Taiwan. [3]Institute of Pioneer Semiconductor Innovations, National Yang Ming Chiao Tung University, Hsinchu, Taiwan. [4]Institue of Electronics, National Yang Ming Chiao Tung University, Hsinchu, Taiwan. [5]Department of Electrical Engineering, Indian Institute of Technology Kanpur, Kanpur, India. [6]Department of Photonics, Institute of Electro-Optical Engineering, National Yang Ming Chiao Tung University, Hsinchu, Taiwan. [7]Department of Electronics and Electrical Engineering, National Yang Ming Chiao Tung University, Hsinchu, Taiwan. [8]Department of Electrical Engineering, National Central University, Taoyuan, Taiwan. ✉email: hckuo0206@nycu.edu.tw; tlwu@nycu.edu.tw; changching.tu@ee.ncu.edu.tw

Immersion cooling, which submerges SiC MOSFETs in electrically insulating oils, offers direct contact and thorough surface cooling[15]. However, it requires a sealed enclosure to prevent leakage, and the dielectric oil may degrade over time, necessitating maintenance and posing contamination risks. Additionally, immersion cooling has limited scalability due to the space needed for immersion tanks. Phase-change cooling technologies, such as vapor chambers[16], heat pipes[17], thermosyphons[18]and two-phase immersion cooling[15,19], are highly efficient methods for managing heat in various applications. These systems rely on the natural process of phase change, where a working fluid evaporates when heated, carrying away heat, and then condenses, releasing it at a cooler location. The heat pipes and thermosyphons use the evaporation and condensation cycle to transfer heat, while the two-phase immersion cooling submerges components in a dielectric fluid that undergoes phase change. The vapor chambers distribute heat evenly across a flat surface, making them ideal for compact spaces. These technologies are generally considered energy-efficient because they do not require external power sources like pumps or fans to move the coolant, relying instead on fluid dynamics. However, their environmental impact depends on factors such as the materials used in manufacturing, the choice of working fluid and the maintenance required, with some coolants potentially being harmful or requiring replacement over time. Overall, phase-change cooling offers a "green" solution. However, the sustainability of phase-change cooling depends on careful material selection and proper system management.

In this work, we demonstrate that the heat generated by a discrete SiC MOSFET conducting a large DC current close to the current rating can be effectively dissipated by water evaporation on the surface of a conventional aluminum heatsink. Without consuming any external power, which we define as zero-power consumption in this work, the liquid water can be transported to the heatsink via cotton ropes and then spread all over the heatsink surface through cellulose paper by means of capillary force. Compared to other phase-change cooling technologies, the setup is simple and cost-effective and only water is consumed during the evaporative cooling process. The comparison between traditional cooling techniques and the evaporative cooling technique proposed in this work is summarized in Table 1. By measuring the on-resistance (R_{ON}) between its drain and source terminals and using the R_{ON} versus junction temperature (T_j) curve, the T_j of the SiC MOSFET can be monitored in real time during the heating process. When the drain current (I_D) is as large as $6\ A$, the T_j is estimated to be $142.7^\circ\ C$, demonstrating that by solely relying on evaporative cooling, the T_j of the SiC MOSFET can be maintained lower than the $T_{j,max}$ ($150^\circ\ C$). Without consuming any power for cooling, the power density of the discrete SiC MOSFET in combination with the evaporative cooling structure is about $1\ W\ g^{-1}$. Lastly, the thermal-fluid-evaporation process taking place on the heatsink surface is investigated in COMSOL. The simulation results are closely matched with experimental data. An efficient heat transfer from the lead frame to the heatsink and an optimized heatsink fin height are identified as the critical steps to further improve the evaporative cooling efficiency.

Evaporative cooling system setup

To demonstrate the effectiveness of the evaporative cooling experiment, the TO-247 lead frame of the discrete SiC MOSFET was tightly screwed to an H-shape aluminum heatsink with a thin layer of heat transfer grease in between. The heatsink outer surface was attached with a layer of cellulous paper (grade 2 quantitative filter paper) and five cotton ropes (5 mm in diameter) were sandwiched between the six cooling fins (Fig. 1(a)). The cotton ropes transport water to the heatsink, while the cellulous paper evenly spreads the water all over the heatsink surface for evaporative cooling (Fig. 1(a) and 1(b)). During the experiment, one end of the cotton rope was constantly immersed in a large beaker of water, while the other end of the cotton rope was directed to another beaker for collecting the transported water. The whole process is facilitated by capillary force without consuming any power. Experimentally, the water flow rate can be obtained by measuring the total mass of water flowing through the cotton ropes over the measurement time ($10\ min$). When the SiC MOSFET is turned off, the water flow rate of the five cotton ropes is $2.84 \pm 0.02\ cm^3\ min^{-1}$ and the cooling fin surface temperature is about the room temperature ($25.1^\circ\ C$), as can be seen in Fig. 1(c). When the SiC MOSFET is conducting a

Cooling Technique	Working Principle	Advantages	Disadvantages	Ref.
Liquid Cooling (with Heatsink)	Forced convection using water pumped through channels to carry away heat	• High cooling efficiency • Suitable for high power density	• Requiring pump, tubing, coolant • Risk of hotspots at low flow	8
Double-Sided Cooling	Heat dissipation from both sides of the device using advanced packaging	• Better temperature uniformity • Reduced thermal resistance	• High complexity in packaging • Reliability concerns due to unmatched thermal expansion	9,10
Immersion Cooling	Devices submerged in dielectric oil for direct and uniform cooling	• Thorough surface cooling • Suitable for high power	• Requiring sealed enclosure • Maintenance issues (fluid degradation) • Limited scalability	15
Phase-Change Cooling (Vapor Chamber, Heat Pipe, Thermosyphon, and Two-phase Immersion)	Heat transferred via phase-change (evaporation and condensation of a working fluid)	• High efficiency • Passive operation • Uniform temperature distribution	• Environmental impact depends on coolant/materials • Potential fluid degradation • Complexity in design and fluid selection	16–19
Proposed Capillary-Driven Evaporative Cooling	Passive water transport through cotton via capillary action, followed by surface evaporation to dissipate heat	• Low-cost • Passive operation • Scalable • Environment friendly (only evaporating water)	• Requiring water reservoir refill • Potential degradation of cellulose paper and cotton ropes in long term	This work

Table 1. Comparison between traditional cooling techniques and the evaporative cooling technique proposed in this work.

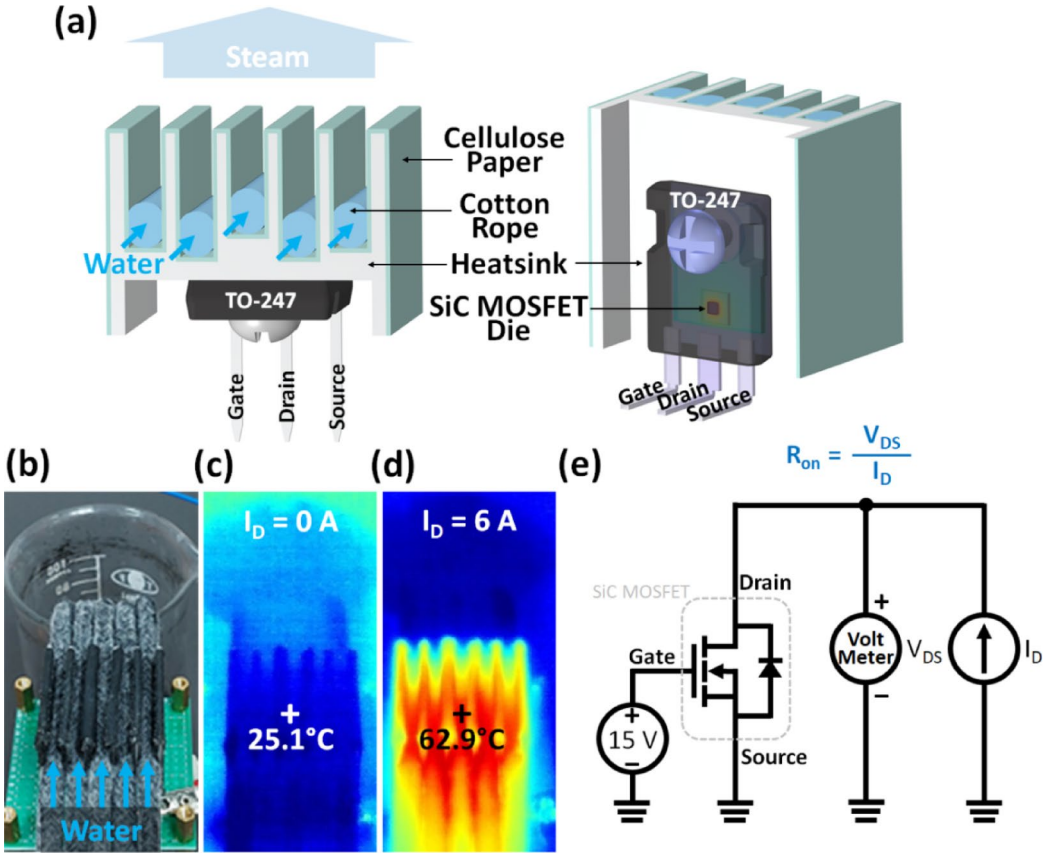

Fig. 1. (**a**) 3D schematic of the discrete SiC MOSFET tightly screwed to the evaporative cooling structure, including the heatsink, cotton ropes and cellulous paper attached to the heatsink surface. The three pins of the TO-247 package are bent 90°, so that the heatsink can face upward for evaporation with the SiC MOSFET discrete affixed to a printed circuit board. **(b)** Bright field image of the heatsink with five cotton ropes. **(c and d)** Thermal images of the heatsink with five cotton ropes when the SiC MOSFET is conducting 0 A and 6 A, respectively. **(e)** Circuit schematic of the SiC MOSFET being biased at $V_{GS} = 15V$ and conducting a constant I_D, which is provided by a DC power supply in the constant current mode. Under this condition, by measuring the V_{DS} with a volt meter, the $R_{ON} = V_{DS} / I_D$ of the SiC MOSFET can be monitored in real time.

constant current of 6 A, the water flow rate increases to $3.87 \pm 0.01\ cm^3\ min^{-1}$ and the cooling fin surface temperature increases to $62.9^\circ\ C$, as can be seen in Fig. 1(d). At this surface temperature, steam rising from the heatsink can be observed by bare eyes. It is worth noting that under the biasing condition of $V_{GS} = 15V$ and constant I_D, which was provided by a DC power supply (GW Instek PLR 20–36) in the constant current mode, by measuring the V_{DS} with a volt meter (GW Instek GDM-8255 A), we can achieve real time monitoring of $R_{ON} = V_{DS}/I_D$ of the SiC MOSFET (Fig. 1(e)).

Device characterizations

The R_{ON} versus T_j curves of the discrete SiC MOSFET ($Wolfspeed$, $C3M0350120D$) were derived from the I_D-V_{DS} curves at $V_{GS} = 15V$, obtained at various T_j values using the Keysight B1500 A semiconductor device parameter analyzer (Fig. 2(a)). The TO-247 lead frame was placed on top of the probe station heating chuck with a thin layer of heat transfer grease in between, while the TO-247 front side was covered by a piece of cotton cloth for reducing convection heat loss. Therefore, the lead frame temperature, measured by a K-type thermocouple, can be approximated as the T_j of the device. Moreover, pulsed IV measurement was applied for minimizing the additional heat generated during the I_D-V_{DS} measurement. Based on the I_D versus V_{DS} curves at different T_j, the R_{ON} versus T_j curves with different I_D can be derived (Fig. 2(b)). Since the SiC MOSFET is biased at a sufficiently large V_{GS} (15 V), the R_{ON} increases as the T_j increases, which is commonly observed for ensuring the current balance among multiple SiC MOSFETs connected in parallel.

Results and discussions

Based on the R_{ON} versus T_j curves in Fig. 2(b), real time monitoring of T_j can be achieved. As an example, after the SiC MOSFET conducted $I_D = 6A$ for $5\ min$, the steady state R_{ON} was measured to be 0.556 Ω and T_j can be estimated as $142.7^\circ\ C$. To systematically investigate the influence of water flow rate on the T_j

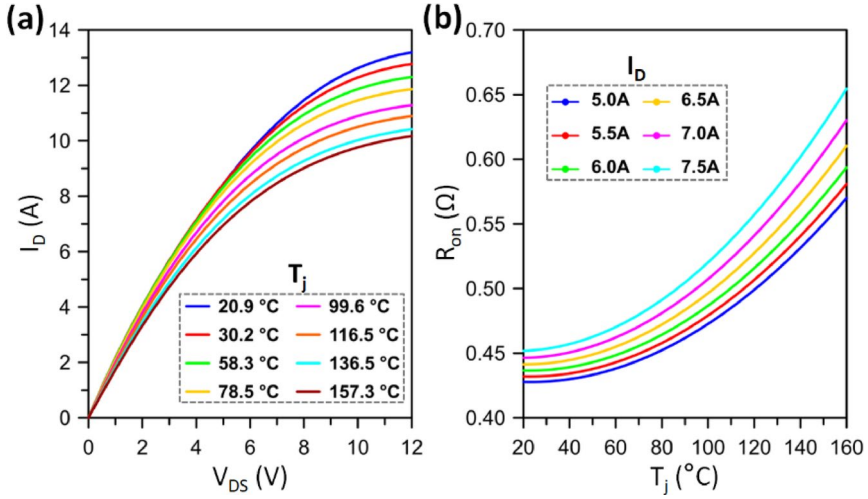

Fig. 2. **(a)** Measured I_D versus V_{DS} curves of the SiC MOSFET discrete at $V_{GS} = 15V$ and different T_j. **(b)** R_{ON} versus T_j curves of the SiC MOSFET discrete at $V_{GS} = 15V$ and different I_D. R_{ON} is equal to the inverse of the slope of I_D versus V_{DS} curve.

at different I_D, in addition to the five cotton ropes mentioned previously, evaporative cooling experiments using three and ten cotton ropes were also conducted. The water flow rates of three and ten cotton ropes are equal to $1.45 \pm 0.01\ cm^3\ min^{-1}$ and $4.01 \pm 0.01\ cm^3\ min^{-1}$ when the SiC MOSFET is off, and increased to be $1.97 \pm 0.02\ cm^3\ min^{-1}$ and $5.63 \pm 0.07\ cm^3\ min^{-1}$ when the SiC MOSFET turns on ($I_D = 6A$), respectively. In addition to the decrease in surface tension, the increase in viscosity is another reason for the increase in water flow rate at elevated temperatures[20].

For comparison, evaporative cooling in a non-zero-power consumption condition is also demonstrated, in which the whole experimental setup is the same, except that an axial AC cooling fan (Sunon, SF11592 A-1092HST.GN, 92 mm × 92 mm × 25 mm) is positioned approximately 5.9 cm above the heatsink to enhance the convection and evaporation. Once the SiC MOSFET turns on, the T_j rapidly increases and enters a steady state in $5\ min$ as shown in Fig. 3(a). With five cotton ropes for water transportation and I_D equal to 5, 5.5 and $6\ A$, the steady state values of T_j are $115.7^\circ\ C$, $127.7^\circ\ C$ and $142.7^\circ\ C$ without cooling fan (zero-power consumption) and $91.6^\circ\ C$, $100.9^\circ\ C$ and $112.1^\circ\ C$ with cooling fan (non-zero-power consumption), respectively. In overall, the T_j can be lowered by about $30^\circ\ C$ with the help of cooling fan. The condition of I_D equal to $7\ A$ with cooling fan (purple solid line in Fig. 3(a)) yields about the same T_j (about $140^\circ\ C$) as the condition of I_D equal to $6\ A$ without cooling fan (green dotted line in Fig. 3(a)).

The steady state powers, power densities and T_j values of the SiC MOSFET conducting I_D ranging from $5\ A$ to $7\ A$ and being cooled by different evaporation conditions are summarized in Fig. 3(b). The dotted straight line follows the equation: $power \times R_{thjc} = T_j - T_c$, where *power* is the conduction loss ($I_D^2 \times R_{on}$) and R_{thjc} is the junction-to-case thermal resistance obtained from the datasheet ($2.5^\circ\ C\ W^{-1}$) and T_c, the TO-247 lead frame temperature, is set as $100^\circ\ C$. For each given power, a data point closer to the dotted straight line means the T_c is closer to $100^\circ\ C$. In general, using cooling fan leads to lower T_j and T_c than not using cooling fan (i.e. zero-power consumption cooling). Furthermore, without cooling fan, using ten cotton ropes (hollow triangles) for water transportation can always yield lower T_j and T_c than using five (hollow stars) and three cotton ropes (hollow crosses). In contrast, when cooling fan is applied to enhance convection and evaporation, five cotton ropes (solid stars) can achieve the lowest T_j and T_c compared to ten (solid triangles) and three cotton ropes (solid crosses). As illustrated by the insets in Fig. 3, compared to five cotton ropes, ten cotton ropes, although having higher water flow rate, suffer from less evaporation area. Therefore, a well balance between the water flow rate and evaporation area is critical to achieve the lowest T_j and T_c at a given power.

To characterize the evaporative cooling efficiency, which is defined as the percentage of total heat ($I_D^2 \times R_{ON}$) dissipated through evaporation, the evaporation rates were measured to be 1.4, 4.9 and $8.1\ mg\ s^{-1}$ for $I_D = 0\ A$ without cooling fan as background, $I_D = 6\ A$ without cooling fan and $I_D = 6\ A$ with cooling fan, respectively. Using the latent heat of water vaporization ($2406\ J\ g^{-1}$ at $40^\circ\ C$)[21], the heat dissipation through evaporation can be calculated as the product of net evaporation rate and latent heat, that is $8.4\ W$ for $I_D = 6\ A$ without cooling fan and $16.1\ W$ for $I_D = 6\ A$ with cooling fan. In other words, out of the total heat generated due to the SiC MOSFET conduction loss, 42% ($= \frac{8.4}{20} \times 100\%$) is dissipated through evaporation for $I_D = 6\ A$ without cooling fan and 89% for $I_D = 6\ A$ with cooling fan. As indicated by the results, the evaporative cooling efficiency can be doubled with the help of cooling fan.

To further investigate the thermal-fluid-evaporation process taking place on the heatsink surface, three-dimensional time-dependent finite element simulation using COMSOL was performed. Four heat transfer behaviors are considered, including solid conduction, air and vapor convections, water evaporation and thermal radiation. Particularly, the incompressible Navier-Stokes equations are solved for the Laminar water flow, which describes the capillary action in the cotton ropes[22]. For modeling the turbulent air flow induced by the cooling

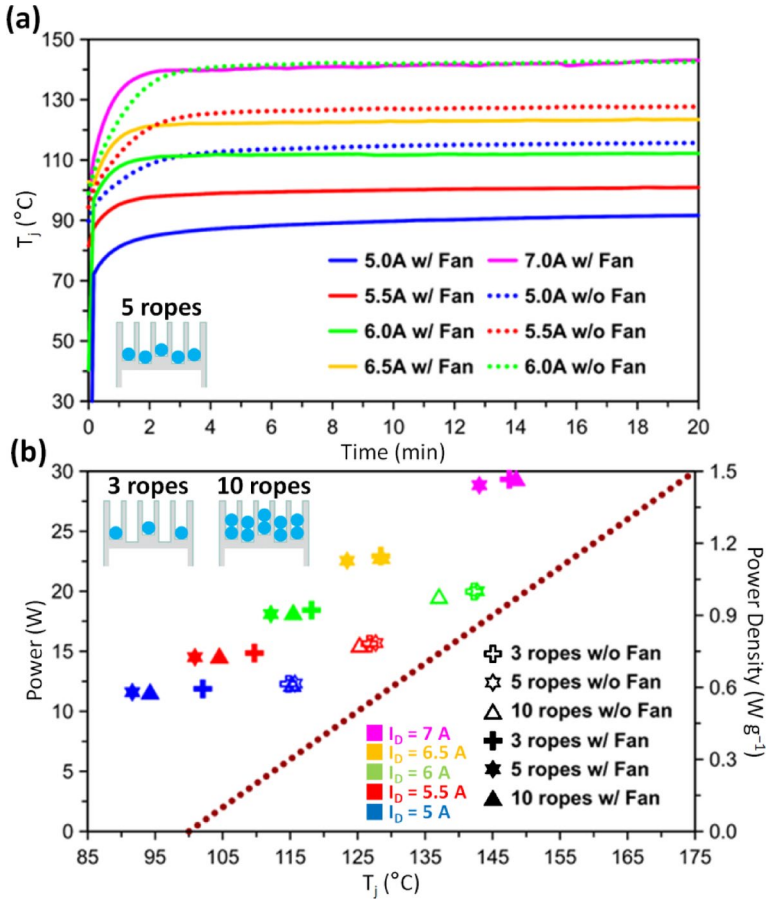

Fig. 3. **(a)** Measured time-dependent T_j of the SiC MOSFET discrete biased at $V_{GS} = 15\ V$ and $I_D = 5\ to\ 7\ A$ ($500\ mA$ steps) and cooled by evaporation using five cotton ropes, with and without cooling fan. **(b)** Measured steady state powers, power densities and T_j values of the SiC MOSFET under various evaporation conditions, including three, five, and ten cotton ropes, with and without cooling fan. The dotted straight line follows the equation: $power \times R_{thjc} = T_j - T_c$, where $R_{thjc} = 2.5^\circ\ C\ W^{-1}$ and $T_c = 100^\circ\ C$.

fan, the $k-\epsilon$ model is used, where k represents the turbulent kinetic energy and ϵ the turbulent dissipation rate[23]. A nonlinear pressure versus volumetric flow rate curve provided by the manufacturer is used to model the cooling fan. The simulated airflow velocity near the heatsink surface ranges from 0.5 to $2.5\ m\ s^{-1}$. To accurately describe the moisture distribution as a result of evaporation, the heat and moisture transport equations with temperature-dependent vapor saturation concentrations are applied[24]. For the thermal radiation from the SiC MOSFET die, the Stefan-Boltzmann equation is used[25], with the surface emissivity assumed to be 0.9 for the package and 0.3 for the heatsink. For modeling the R_{thjc} of the TO-247 package, the following layers were considered: $350\ \mu\ m$ SiC substrate ($380\ W\ m^{-1}K^{-1}$)[26], $4\ \mu\ m$ Al bonding pad ($247\ W\ m^{-1}K^{-1}$)[27], $50\ \mu\ m$ die soldering layer ($57\ W\ m^{-1}K^{-1}$)[28], and $1\ mm$ Al lead frame ($247\ W\ m^{-1}K^{-1}$). The package encapsulant has a relatively low thermal conductivity of $0.25\ W\ m^{-1}K^{-1}$[29]. For heat conduction calculation, although the cellulose paper ($0.076\ W\ m^{-1}K^{-1}$) and cotton rope ($0.059\ to\ 0.082\ W\ m^{-1}K^{-1}$) in dry condition are thermal insulating[30,31], they are permeated with water during operation. Therefore, a thermal conductivity close to liquid water ($0.603\ W\ m^{-1}K^{-1}$) was used in modeling the wet cellulose paper and cotton ropes.

Next, we present the thermal images of the discrete SiC MOSFETs after conducting $I_D = 6\ A$ for 1, 2.5 and $5\ min$ without and with cooling fan in Fig. 4(a) and 4(b), respectively. At $5\ min$, the hot spot corresponds to the location of the SiC MOSFET die. Furthermore, a package temperature difference of $28.7^\circ\ C$ between the conditions with ($45.8^\circ\ C$) and without cooling fan ($74.5^\circ\ C$) was observed. This result is close to the T_j difference between the conditions with cooling fan ($112.1^\circ\ C$, green solid star in Fig. 3(b)) and without cooling fan ($142.7^\circ\ C$, green hollow star in Fig. 3(b)). Most importantly, under the same condition ($I_D = 6\ A$ and five cotton ropes for water transportation), the COMSOL simulation results are closely matched with the experimental results (Fig. 4(c)-(d)). Furthermore, the simulated T_j at different time points after conducting $I_D = 6\ A$ are consistent with the experimental T_j versus time curves (Fig. 4(e)). It is worth noting that the evaporative cooling efficiency can be influenced by several factors collectively. Therefore, instead of focusing on one parameter, we performed another simulation with multiple key parameters varying in certain ranges,

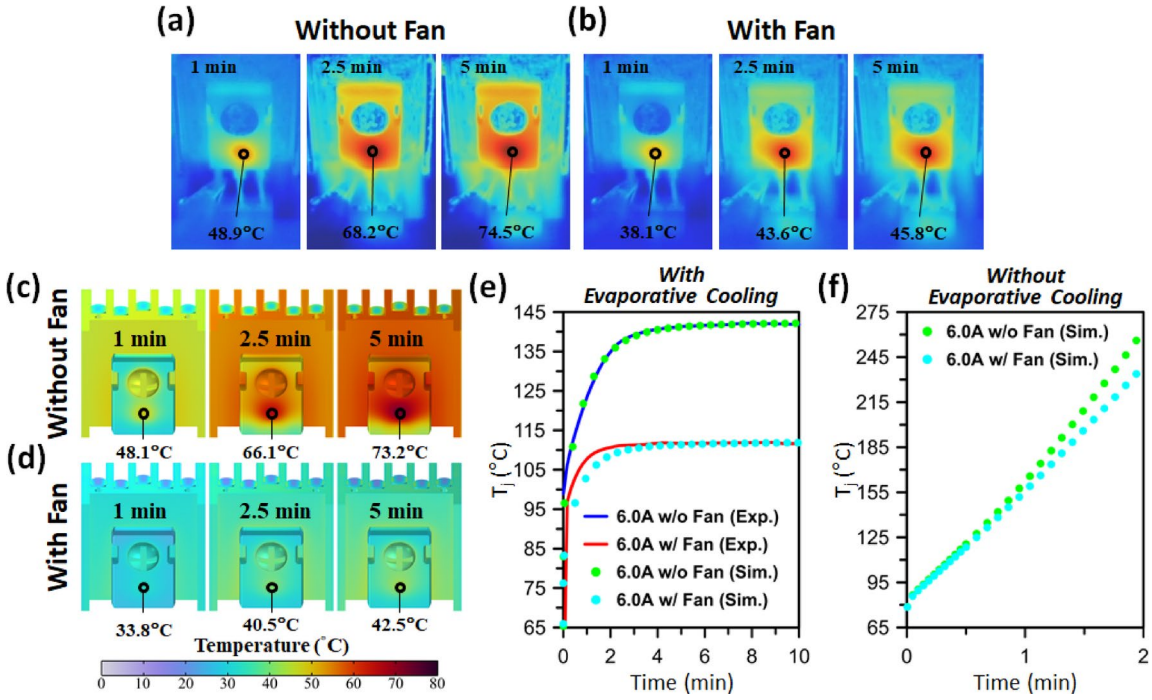

Fig. 4. Experimental thermal images of the SiC MOSFET discrete after conducting $I_D = 6\ A$ for $1,\ 2.5$ and $5\ min$ without **(a)** and with **(b)** cooling fan and using five cotton ropes for water transportation. **(c and d)** Simulated thermal images under the same conditions as (a) and (b). **(e)** Experimental and simulated time-resolved T_j of the SiC MOSFET after conducting $I_D = 6\ A$ with and without cooling fan. Here the experimental time-resolved curves are reproduced from the solid (with cooling fan) and dashed (without cooling fan) green lines in Fig. 3 (a). **(f)** Simulated time-resolved T_j of the SiC MOSFET after conducting $I_D = 6\ A$ with and without cooling fan. Here the cellulose paper and cotton ropes are removed for modeling the condition without evaporative cooling.

including the ambient temperature ($24 \pm 0.5^\circ C$), the inlet water temperature ($23 \pm 0.5^\circ C$), the relative humidity ($45 \pm 5\%$), and the water flow rate ($3.9 \pm 0.1\ cm^3\ min^{-1}$). The resulting T_j showed a lightly skewed distribution, with the maximum at $145.9^\circ C$, the minimum at $141.0^\circ C$, the average at $143.0^\circ C$ and the standard deviation equal to $0.9^\circ C$.

The heatsink design plays a significant role in cooling. How efficiently a heatsink dissipates heat can be characterized by the heatsink surface-to-ambient thermal resistance (R_{thsa}), which can be calculated by using the equation: $R_{thsa} = (T_j - T_a - P_d \times R_{thjs})/P_d$[32], where T_a is the ambient temperature ($24^\circ C$), P_d is the thermal power generated by the SiC MOSFET ($I_D^2 \times R_{on}$), and R_{thjs} is the junction-to-heatsink surface thermal resistance ($3.1\ K\ W^{-1}$). Based on the T_j in Fig. 4(e) and the R_{ON} versus T_j curve in Fig. 2(b), the simulated R_{thsa} after conducting $I_D = 6\ A$ for $2\ min$ is equal to 1.6 and $2.3\ K\ W^{-1}$ with and without cooling fan, respectively. In contrast, when the cellulose paper and cotton ropes are removed, i.e. without the evaporative cooling, under the same condition, the simulated R_{thsa} significantly increases to 4.6 and $4.9\ K\ W^{-1}$ with and without cooling fan, respectively. Moreover, without the evaporative cooling, the T_j surges to well above $T_{j,max}$ immediately after the SiC MOSFET turning on and continues to increase (Fig. 4(f)).

Moreover, based on the cross-sectional temperature distributions, the heat transfer between the lead frame and heatsink is identified as the critical step for further improving the evaporative cooling efficiency. Regardless of cooling fan, a nearly constant temperature difference of about $11^\circ C$ is observed between the lead frame and heatsink (Fig. 5(a)). For experiment, a thin layer of heat transfer grease with a thermal conductivity of $4\ W\ m^{-1}K^{-1}$ was applied between the lead frame and heatsink. For the COMSOL simulation in Fig. 4(c)-(e) and 5(a), the thermal conductivity of the heat transfer grease was also set to be $4\ W\ m^{-1}K^{-1}$ and the film thickness was assumed to be $100\ \mu\ m$. Next, the influence of the thermal conductivity of the heat transfer grease is investigated (Fig. 5(b)). For the SiC MOSFET conducting $I_D = 6\ A$ without cooling fan, the temperature difference between the lead frame and heatsink decreases from $12.1^\circ C$ to $4^\circ C$ as the thermal conductivity increases from $4\ W\ m^{-1}K^{-1}$ to $20\ W\ m^{-1}K^{-1}$. For the thermal conductivity larger than $2\ W\ m^{-1}K^{-1}$, the T_j can be kept lower than $T_{j,max}$ ($150^\circ C$).

Lastly, the potential scalability of the zero-power consumption evaporative cooling is demonstrated using COMSOL simulation (Fig. 6), in which the key parameters are pre-calibrated as in Fig. 4. Three SiC MOSFET discretes are placed in parallel, sharing one heatsink (length = $87\ mm$, width = $30\ mm$ and height = $22\ mm$) and adopting a similar evaporative cooling scheme as for the single SiC MOSFET discrete in Fig. 1(a). Another module of three SiC MOSFET discretes is placed in close proximity. With the two modules facing each other, the cooling water is flowing from two sides to the center through cotton ropes. Each SiC MOSFET conducts

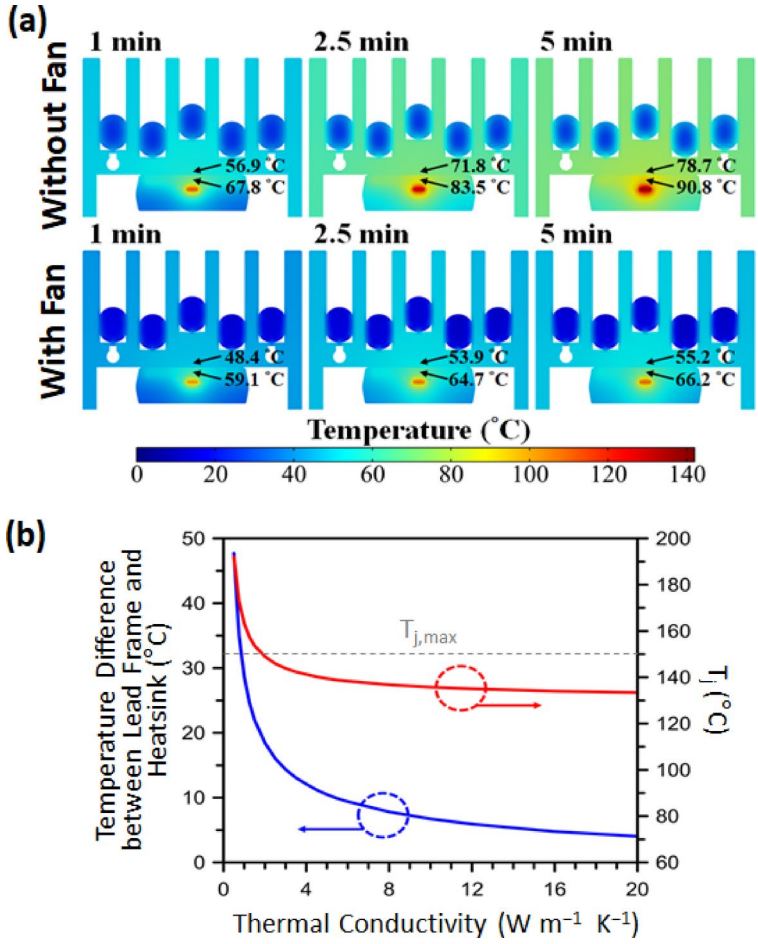

Fig. 5. **(a)** Simulated cross sectional temperature distributions of the SiC MOSFET discrete after conducting $I_D = 6\ A$ for 1, 2.5 and $5\ min$ without and with cooling fan. **(b)** Simulated temperature difference between the lead frame and heatsink (blue line) and simulated T_j (red line) for the SiC MOSFET discrete conducting $I_D = 6\ A$ without cooling fan as a function of the thermal conductivity of the heat transfer grease. The evaporative cooling is based on five cotton ropes.

$I_D = 6\ A$, generating heat about $20\ W$. In other words, a total $120\ W$ of heat, which is equivalent to the power loss of a $12\ kW$ converter with 99% efficiency, can be dissipated by the evaporative cooling system. Moreover, we found that with only one layer of cotton ropes (15 lines for one module), the T_j can be reduced from $140.2^\circ\ C$ to $132.6^\circ\ C$, if the heatsink fin height is increased from original $14\ mm$ to $44\ mm$ (Fig. 6(c)). More impressively, when using two layers of cotton ropes (30 lines for one module), the T_j can be further lowered to $129.9^\circ\ C$ and $124.8^\circ\ C$ with the heatsink fin height equal to 14 mm and 44 mm, respectively. While the above simulation demonstrates scalability, some limitations of the evaporative cooling system should be addressed. First, once the absorption of water of a cotton rope reaches saturation, its fluid transport efficiency may no longer exhibit further improvement. When dissipating high power of heat, in order to achieve low T_j, a larger number of cotton ropes are necessary (Fig. 6(c)). Second, prolonged exposure to water and other environmental factors (such as air pollutants and microorganisms) at elevated temperatures may cause degradations of the cellulose paper and cotton ropes. Therefore, for better reliability, it is important to explore novel water transporting materials with high water absorption capacity and long-term stability.

Conclusion

The proposed evaporative cooling system effectively dissipates heat in SiC MOSFETs operating at high currents, maintaining the junction temperature (T_j) well below the rated maximum junction temperature ($T_{j,max}$) without consuming additional power. Experimental and COMSOL simulation results validate the efficacy of the cooling system, emphasizing the importance of optimizing water flow rates, lead frame-to-heatsink heat transfer and heatsink fin height. The inclusion of a cooling fan further improves cooling efficiency, demonstrating the system's adaptability to varying power demands. This innovative cooling strategy holds promise for energy-efficient thermal management in advanced high-power semiconductor devices and modules.

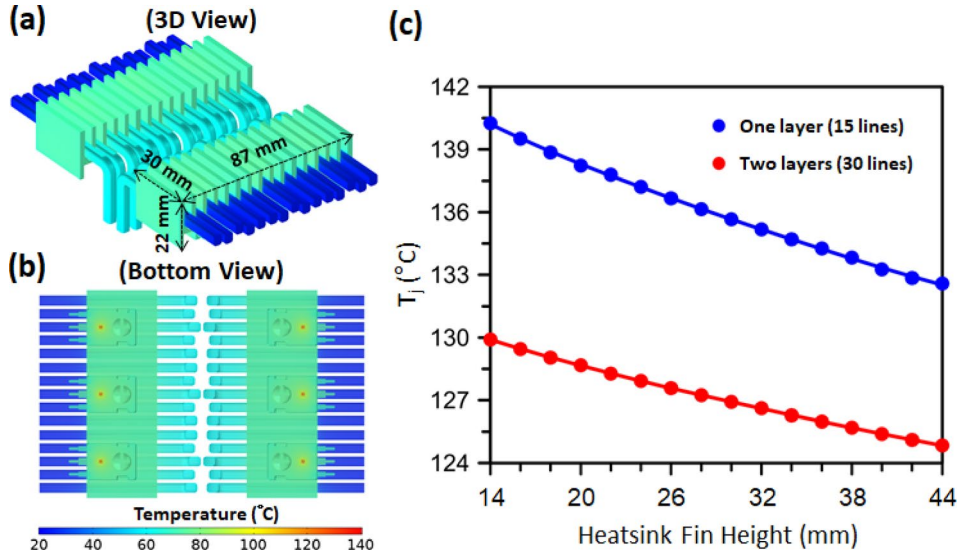

Fig. 6. **(a)** 3D view and **(b)** bottom view of the two evaporative cooling modules for six SiC MOSFETs, each conducting $I_D = 6\ A$ and generating heat about $20\ W$. With the two modules facing each other, the cooling water is flowing from two sides to the center through cotton ropes and capillary force. **(c)** Simulated T_j versus heatsink fin height for the evaporative cooling modules using one layer (blue line) and two layers (red line) of cotton ropes.

Data availability

The datasets generated and/or analyzed during the current study are available from the corresponding author on reasonable request.

Received: 7 February 2025; Accepted: 2 May 2025
Published online: 10 May 2025

References

1. Nakayama, W., Suzuki, O., Hara, Y. & Conference, P. Thermal management of electronic and electrical devices in automobile environment, 2009 IEEE Vehicle Power and Dearborn, MI, USA, pp. 601–608, (2009). https://doi.org/10.1109/VPPC.2009.5289792
2. Taha, W., Nahid-Mobarakeh, B., Bauman, J. & Expo Efficiency evaluation of 2L and 3L SiC-based traction inverters for 400V and 800V electric vehicle powertrains, 2021 IEEE Transportation Electrification Conference (ITEC), Chicago, IL, USA, pp. 625–632, (2021). https://doi.org/10.1109/ITEC51675.2021.9490082
3. Tu, C. C. et al. Industry perspective on power electronics for electric vehicles. *Nat. Reviews Electr. Eng.* **1**, 435–452. https://doi.org/10.1038/s44287-024-00055-4 (2024).
4. Zhu, J. et al. IEEE Applied Power Electronics Conference and High efficiency SiC traction inverter for electric vehicle applications, (APEC), San Antonio, TX, USA, 2018, pp. 1428–1433, (2018). https://doi.org/10.1109/APEC.2018.8341204
5. Gurpinar, E. et al. SiC MOSFET-based power module design and analysis for EV traction systems, 2018 IEEE Energy Conversion Congress and (ECCE), Portland, OR, USA, pp. 1722–1727, (2018). https://doi.org/10.1109/ECCE.2018.8557609
6. Liu, G. et al. Comparison of SiC MOSFETs and GaN HEMTs based high-efficiency high-power-density 7.2 kW EV battery chargers, 2017 IEEE 5th Workshop on Wide Bandgap Power Devices and Applications (WiPDA), Albuquerque, NM, USA, pp. 391–397, (2017). https://doi.org/10.1109/WiPDA.2017.8170579
7. Huang, Z. H., Tang, S. W., Fan, C. T., Lin, M. C. & Wu, T. L. Dynamic on-resistance stability of SiC and GaN power devices during high-frequency (100–300 kHz) hard switching and zero voltage switching operations. *Microelectron. Reliab.* **145**, 114983. https://doi.org/10.1016/j.microrel.2023.114983 (2023).
8. Catuneanu, J. G., Burgers, P., Fleury, W. J., Zhang & Tung Ng, W. Practical limits of liquid cooling electric vehicle power modules, 33rd International Symposium on Power Semiconductor Devices and ICs (ISPSD), Nagoya, Japan, 2021, pp. 379–382, (2021). https://doi.org/10.23919/ISPSD50666.2021.9452221
9. Pai, P. et al. SiC MOSFET-based high performance double side cooled module and compact cooler for high power-density automotive inverter applications, 2022 IEEE International Workshop on Integrated Power Packaging (IWIPP), Grenoble, France, 2022, pp. 1–6. https://doi.org/10.1109/IWIPP50752.2022.9894198
10. Chen, Y., Lei, G., Lu, G. Q. & Mei, Y. H. High-temperature characterizations of a half-bridge wire-bondless SiC MOSFET module. *IEEE J. Electron. Devices Soc.* **9**, 966–971. https://doi.org/10.1109/JEDS.2021.3119428 (2021).
11. Sugiura, K. et al. Reliability evaluation of SiC power module with sintered ag die attach and stress-relaxation structure. *IEEE Trans. Compon. Packag. Manuf. Technol.* **9**, 609–615. https://doi.org/10.1109/TCPMT.2019.2901543 (2019).
12. Jeon, J. et al. Finite element and experimental analysis of spacer designs for reducing the thermomechanical stress in double-sided cooling power modules. *IEEE J. Emerg. Sel. Top. Power Electron.* **9**, 3883–3891. https://doi.org/10.1109/JESTPE.2020.2998546 (2021).
13. Chen, Y., Mei, Y. H., Ning, P. & Lu, G. Q. Local interconnection degradation of a double-sided cooling SiC MOSFET module under power cycling. *IEEE Trans. Compon. Packag. Manuf. Technol.* **14**, 832–840. https://doi.org/10.1109/TCPMT.2023.3347445 (2024).
14. Zheng, H., Ngo, K. D. T. & Lu, G. Q. Temperature cycling reliability assessment of die attachment on bare copper by pressureless nanosilver sintering. *IEEE Trans. Device Mater. Reliab.* **15**, 214–219. https://doi.org/10.1109/TDMR.2015.2417114 (2015).
15. Yang, F., Liu, C. & Shen, J. Immersion oil cooling method of discrete SiC power device in electric vehicle, *2022 IEEE Energy Conversion Congress and Exposition (ECCE)*, Detroit, MI, USA, pp. 1–5, (2022). https://doi.org/10.1109/ECCE50734.2022.9948112

16. Li, Y., Chen, X., Wang, Y., Li & Yan, Y. Heat spreading performance of SiC-based power module with bonded vapour chamber for electric powertrain integration. *Appl. Therm. Eng.* **181**, 115896. https://doi.org/10.1016/j.applthermaleng.2020.115896 (2020).
17. Weng, Y. C., Cho, H. P., Chang, C. C. & Chen, S. L. Heat pipe with PCM for electronic cooling. *Appl. Energy*. **88**, 1825–1833. https://doi.org/10.1016/j.apenergy.2010.12.004 (2011).
18. Acharya, S., Anurag, A., Bhattacharya, S. & Pellicone, D. Performance evaluation of a loop thermosyphon-based Heatsink for high-power SiC-based converter applications. *IEEE Trans. Compon.* **10**, 99–110. https://doi.org/10.1109/TCPMT.2019.2923332 (2020). Packaging and Manufacturing Technology.
19. Pandey, H. et al. Two-phase immersion cooler for medium-voltage silicon carbide MOSFETs,., *23rd IEEE Intersociety Conference on Thermal and Thermomechanical Phenomena in Electronic Systems (ITherm)*, Aurora, CO, USA, 2024, pp. 1–6, (2024). https://doi.org/10.1109/ITherm55375.2024.10709426
20. Buffone, K., Sefiane & Christy, J. R. E. Experimental investigation of self-induced thermocapillary convection for an evaporating meniscus in capillary tubes using micro–particle image velocimetry. *Phys. Fluids*. **17** (5). https://doi.org/10.1063/1.1901688 (2005).
21. Monteith, J. L. Latent heat of vaporization in thermal physiology. *Nat. New. Biology*. **236**, 96. https://doi.org/10.1038/newbio236096a0 (1972).
22. Mohamed, M. S. Discrete exterior calculus discretization of incompressible Navier-Stokes equations over surface simplicial meshes. *J. Comput. Phys. Vol.* **312**, 175–191. https://doi.org/10.1016/j.jcp.2016.02.028 (2016).
23. N. G. Wright, and G. J. Easom, Non-linear k–ε turbulence model results for flow over a Building at full-scale. *Appl. Math. Modelling Vol* **27**, pp. 1013–1033, (2003). https://doi.org/10.1016/S0307-904X(03)00123-9
24. J. Berger, D., Mendes & Rysbaiuly, B. A new model for simulating heat, air and moisture transport in porous Building materials. *Int. J. Heat. Mass. Transf. Vol.* **134**, 1041–1060. https://doi.org/10.1016/j.ijheatmasstransfer.2019.01.025 (2019).
25. Kerschbaumer, N. M., Niedermaier, S., Lohmüller, T. & Feldmann, J. Contactless and spatially structured cooling by directing thermal radiation. *Sci. Rep. Vol.* **11**, 16209. https://doi.org/10.1038/s41598-021-95606-2 (2021).
26. Li, L., Fukui, A. & Wakejima, A. Bonding GaN on high thermal conductivity graphite composite with adequate interfacial thermal conductance for high power electronics applications. *Appl. Phys. Lett.* **116**, 142105. https://doi.org/10.1016/j.applthermaleng.2020.115896 (2020).
27. Godbole, K., Bhushan, B., Murty, S. N. & Mondal, K. Al-Si controlled expansion alloys for electronic packaging applications. *Prog. Mater. Sci.* **114**, 101268. https://doi.org/10.1016/j.pmatsci.2024.101268 (2024).
28. Zhao, K. et al. Mechanical properties and microstructure of large-area diamond/silicon bonds formed by pressure-assisted silver sintering for thermal management. *Mater. Today Commun.* **34**, 105230. https://doi.org/10.1016/j.mtcomm.2022.105230 (2023).
29. Hsieh, Y. High thermal conductivity epoxy molding compound filled with a combustion synthesized AlN powder. *J. Appl. Polym. Sci.* **102**, 4734–4740. https://doi.org/10.1002/app.25000 (2006).
30. Dombek, G. et al. Effect of moisture on the thermal conductivity of cellulose and aramid paper impregnated with various dielectric liquids. *Energies* **13**, 4433. https://doi.org/10.3390/en13174433 (2020).
31. Asdrubali, F., D'Alessandro & Schiavoni, S. A review of unconventional sustainable Building insulation materials. *Sustainable Mater. Technol.* **4**, 1–17. https://doi.org/10.1016/j.susmat.2015.05.002 (2015).
32. Christen, D., Stojadinovic, M. & Biela, J. Energy efficient heat sink design: natural versus forced convection cooling. *IEEE Trans. Power Electron.* **32**, 8693–8704. https://doi.org/10.1109/TPEL.2016.2640454 (2017).

Acknowledgements

This work was supported in part by the National Science and Technology Council (NSTC), Taiwan, under Grant 112-2628-E-A49-020-MY3, 113-2218-E-008-012-, 113-2218-E-A49-018, 113-2640-E-008-002- and 113-2222-E-008-010-, and in part by the "Advanced Semiconductor Technology Research Center" from the Featured Areas Research Center Program within the framework of the Higher Education Sprout Project by the Ministry of Education (MOE) in Taiwan.

Author contributions

K.B.H., C.S., Y.S.H. and C.C.T. conducted experiments, analyzed data and prepared figures. K.B.H. performed simulations. K.B.H., S.K.S. and C.C.T. wrote the main manuscript. Y.K.H., Y.S.C. and H.C.K. provided supervision and validated data. T.L.W. and C.C.T. revised and submitted the manuscript. All authors reviewed the manuscript.

Declarations

Competing interests

The authors declare no competing interests.

Additional information

Correspondence and requests for materials should be addressed to H.-C.K., T.-L.W. or C.-C.T.

Reprints and permissions information is available at www.nature.com/reprints.

Publisher's note Springer Nature remains neutral with regard to jurisdictional claims in published maps and institutional affiliations.

Open Access This article is licensed under a Creative Commons Attribution-NonCommercial-NoDerivatives 4.0 International License, which permits any non-commercial use, sharing, distribution and reproduction in any medium or format, as long as you give appropriate credit to the original author(s) and the source, provide a link to the Creative Commons licence, and indicate if you modified the licensed material. You do not have permission under this licence to share adapted material derived from this article or parts of it. The images or other third party material in this article are included in the article's Creative Commons licence, unless indicated otherwise in a credit line to the material. If material is not included in the article's Creative Commons licence and your intended use is not permitted by statutory regulation or exceeds the permitted use, you will need to obtain permission directly from the copyright holder. To view a copy of this licence, visit http://creativecommons.org/licenses/by-nc-nd/4.0/.

© The Author(s) 2025